Upper limits for neutrino oscillations $\bar{\nu}_\mu \to \bar{\nu}_e$ from muon decay at rest

B. Armbruster,[1] I. M. Blair,[2] B. A. Bodmann,[3] N. E. Booth,[4] G. Drexlin,[1] J. A. Edgington,[2] C. Eichner,[5] K. Eitel,[1] E. Finckh,[3] H. Gemmeke,[6] J. Hößl,[3] T. Jannakos,[1] P. Jünger,[3] M. Kleifges,[6] J. Kleinfeller,[1] W. Kretschmer,[3] R. Maschuw,[1,5] C. Oehler,[1] P. Plischke,[1] J. Reichenbacher,[1] C. Ruf,[5] M. Steidl,[1] J. Wolf,[7] and B. Zeitnitz[1,7]

(KARMEN Collaboration)

[1]Institut für Kernphysik, Forschungszentrum Karlsruhe, Postfach 3640, D-76021 Karlsruhe, Germany
[2]Physics Department, Queen Mary, University of London, Mile End Road, London E1 4NS, United Kingdom
[3]Physikalisches Institut, Universität Erlangen-Nürnberg, Erwin Rommel Strasse 1, D-91058 Erlangen, Germany
[4]Department of Physics, University of Oxford, Keble Road, Oxford OX1 3RH, United Kingdom
[5]Institut für Strahlen und Kernphysik, Universität Bonn, Nußallee 14-16, D-53115 Bonn, Germany
[6]Institut für Prozessdatenverarbeitung und Elektronik, Forschungszentrum Karlsruhe, Postfach 3640, D-76021 Karlsruhe, Germany
[7]Institut für experimentelle Kernphysik, Universität Karlsruhe, Gaedestrasse 1, D-76128 Karlsruhe, Germany

(Received 8 March 2002; published 5 June 2002)

The KARMEN experiment at the spallation neutron source ISIS used $\bar{\nu}_\mu$ from μ^+ decay at rest for the search of neutrino oscillations $\bar{\nu}_\mu \to \bar{\nu}_e$ in the appearance mode, with $p(\bar{\nu}_e, e^+)n$ as a detection reaction of $\bar{\nu}_e$. In total, 15 candidates satisfy all conditions for the $\bar{\nu}_e$ signature, in agreement with the background expectation of 15.8 ± 0.5 events, yielding no indication for oscillations. A single event based likelihood analysis leads to upper limits on the oscillation parameters $\sin^2(2\Theta) < 1.7 \times 10^{-3}$ for $\Delta m^2 \geqslant 100$ eV^2 and $\Delta m^2 < 0.055$ eV^2 for $\sin^2(2\Theta) = 1$ at 90% confidence. Thus, KARMEN does not confirm the LSND experiment and restricts significantly its favored parameter region for $\bar{\nu}_\mu \to \bar{\nu}_e$.

DOI: 10.1103/PhysRevD.65.112001 PACS number(s): 14.60.St, 14.60.Pq, 25.30.Pt

I. INTRODUCTION

The study of neutrino masses and mixing originating from extensions of the standard model (SM) is one of the most interesting issues in particle physics which has also considerable impact on astrophysical and cosmological problems. For example, neutrino masses in the range of a few eV would mean a significant contribution to the matter content in the universe. In addition, understanding the mass and mixing scheme of neutrinos is a very promising tool to improve our knowledge on mass generating mechanisms for all elementary particles.

A very sensitive way of probing neutrino masses and the mixing between different neutrino flavors is the search for neutrino oscillations. The experimental progress in this field during recent years has been remarkable, yielding strong evidence for neutrino oscillations from investigations of solar and atmospheric neutrinos. The long-standing problem of the solar ν deficit, observed by different experiments [1] including the latest results from the Sudbury Neutrino Observatory (SNO) [2], is consistently explained as the transition of ν_e into other active neutrino flavors [3,4]. In addition, the atmospheric neutrino anomaly gives evidence for neutrino oscillations, namely, for $\nu_\mu \to \nu_x$ disappearance oscillations [5]. Because of the precision measurements of the Super-Kamiokande experiment, the oscillation channel $\nu_\mu \to \nu_\tau$ is strongly favored [6].

Despite the convincing results from solar and atmospheric ν-oscillation experiments, all indications for oscillations are obtained by searches in the *disappearance* mode. Up to now, there is only one piece of evidence for ν-oscillations in the *appearance* mode: The LSND (Liquid Scintillator Neutrino Detector) experiment [7] at the Los Alamos Neutron Science Center (LANSCE) reported 1995 initial results of the search for $\bar{\nu}_\mu \to \bar{\nu}_e$ oscillations with $\bar{\nu}_\mu$ produced in μ^+ decays at rest [8]. Supported by a positive signal in the $\nu_\mu \to \nu_e$ channel [9], updates with increased statistics [10,11] underlined the evidence of an observed $\bar{\nu}_e$ excess but also reduced the original signal strength. The $\bar{\nu}_e$ signal is explained as originating from $\bar{\nu}_\mu \to \bar{\nu}_e$ oscillations with an oscillation probability $P = (0.264 \pm 0.067 \pm 0.045)\%$ [12].

Because of the sensitivity region of LSND, these findings suggest rather high mass differences of $\Delta m^2 > 0.1$ eV^2, which would imply significant contributions of neutrinos to the cosmological problem of dark matter. Because of the high Δm^2 scale it is not possible to accommodate all three evidences (solar, atmospheric, LSND) with their distinct regions of Δm^2 within the framework of the SM with its three neutrino flavors, extended by allowing for nonzero neutrino masses. Proposed solutions to this problem include, e.g., the incorporation of a sterile neutrino state [13–15], supersymmetry [16], or *CPT* violation [17]. These deep impacts on particle and astrophysical aspects therefore require a thorough and independent test of the $\bar{\nu}_\mu \to \bar{\nu}_e$ evidence of LSND.

This paper describes the search for $\bar{\nu}_\mu \to \bar{\nu}_e$ oscillations by the KARMEN (Karlsruhe Rutherford Medium Energy Neutrino) experiment, which was located at the highly pulsed spallation neutron source ISIS of the Rutherford Laboratory (U.K.). The results presented here are based on the final data set recorded with the full experimental setup of KARMEN 2 from February 1997 until March 2001.

The KARMEN experiment took data, in a different experimental configuration (KARMEN 1), since 1990. In this first period, the data analysis was focused on the investigation of neutrino-nucleus interactions [18–20], but also on the search for the oscillation channels $\nu_\mu \rightarrow \nu_e$ [21] and $\nu_e \rightarrow \nu_x$ [22]. Other searches of nonstandard model physics such as new particles in pion decay [23], lepton flavor violating pion and muon decays [24], or non-*V-A* contributions to the muon decay $\mu^+ \rightarrow e^+ + \nu_e + \bar{\nu}_\mu$ [25] were also performed. Here, we report on the most sensitive channel, the search for $\bar{\nu}_\mu \rightarrow \bar{\nu}_e$ oscillations.

The paper is organized as follows. Section II describes the neutrino source ISIS and the KARMEN detector, after which, in Sec. III, the $\bar{\nu}_\mu \rightarrow \bar{\nu}_e$ oscillation signature is presented. Section IV defines some general event requirements for the identification of $\bar{\nu}_e$-induced events in the data analysis. We discuss the background in Sec. V. The final event sample together with the final data cuts and background expectations is given in Sec. VI. The data analysis is described in detail in Sec. VII together with the presentation of the final $\bar{\nu}_\mu \rightarrow \bar{\nu}_e$ results. A detailed discussion of the results with respect to the LSND evidence and the negative results from other experiments follows in Sec. VII C.

II. EXPERIMENTAL CONFIGURATION

A. The neutrino source ISIS

The pulsed spallation neutron source ISIS of the Rutherford Appleton Laboratory uses a rapid cycle synchrotron to accelerate protons up to 800 MeV with a design beam current of $I = 200$ μA. The protons are extracted from the synchrotron with a repetition frequency of 50 Hz as a double pulse, consisting of two parabolic pulses, with a width of 100 ns and being separated 325 ns in time. When the 800 MeV protons hit the water cooled Ta-D_2O target $(0.0448 \pm 0.0030)\pi^+$ per incident proton are produced [26]. Production of three distinct neutrino flavors ν_μ, ν_e and $\bar{\nu}_\mu$ occurs via the $\pi^+ - \mu^+$ decay chain in the beam stop:

$$\pi^+ \longrightarrow \mu^+ + \nu_\mu \qquad \tau_\pi = 26\ ns$$

$$\mu^+ \longrightarrow e^+ + \nu_e + \bar{\nu}_\mu \qquad \tau_\mu = 2.2\ \mu s$$

The π^+ and μ^+ are stopped within the heavy target and decay at rest. The unique time structure of the ISIS proton pulse allows a clear separation of ν_μ induced events from $\bar{\nu}_\mu$ and ν_e induced events. Because of the short lifetime of π^+ ($\tau = 26$ ns) the ν_μ production closely follows the ISIS proton beam profile. One therefore expects two ν_μ bursts within the first 600 ns after the extraction of the proton beam. The 2-body decay at rest of π^+ leads to monoenergetic ν_μ with an energy of $E_{\nu_\mu} = 29.8$ MeV. Studies of these ν_μ are published in Ref. [20]. On the other hand, the $\bar{\nu}_\mu$ and ν_e from μ^+ decay are expected to emerge on a time scale of a few μs due to the μ^+ lifetime of $\tau = 2.2$ μs. The time spectrum of $\bar{\nu}_\mu$ and ν_e induced events [see Fig. 1 (a)] reflects the lifetime of μ^+ and thus contains additional information to discriminate in the data analysis versus background reactions. The $\bar{\nu}_\mu$ and ν_e from muon decay have continuous energy spectra (see Fig. 1). The energy spectra are well defined and can be calculated precisely because of the decay at rest kinematics and the simple *V-A* structure of the μ^+ decay. From the three neutrino flavors, which are produced with equal intensity and emitted isotropically, the highest mean energy is obtained by the $\bar{\nu}_\mu$, which have the maximum intensity at the end point energy of 52.8 MeV.

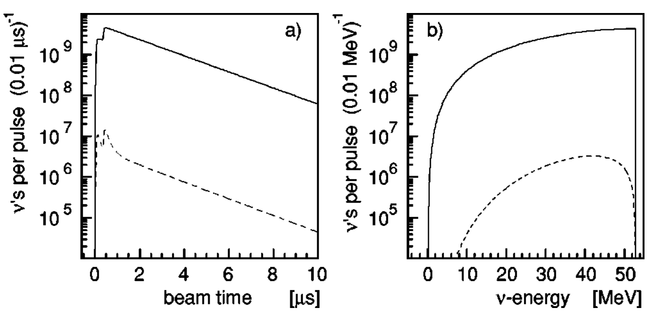

FIG. 1. (a) Time and (b) energy distribution of neutrinos at the ISIS beam stop for a beam current of $I = 200$ μA: $\bar{\nu}_\mu$ from μ^+ decay (solid), $\bar{\nu}_e$ from μ^- decay (dashed).

The intrinsic contamination of the ISIS ν beam with $\bar{\nu}_e$ is very small. The suppression of $\bar{\nu}_e$ production follows from the following factors: The stopping of 800 MeV protons in the Ta-D_2O target produces less π^- than π^+ $(\pi^-/\pi^+ = 0.56)$. While π^- , which are stopped quickly (<1 ns), mainly undergo nuclear capture, it is only a fraction of 1.2% which decay in flight and therefore become of relevance for the $\bar{\nu}_e$ contamination. The following μ^- decay at rest in the target station again is suppressed by the efficient muon capture (93% of μ^- produced) on the high *Z* material of the spallation target. This π^--μ^- decay chain leads to a very small contamination of $\bar{\nu}_e/\bar{\nu}_\mu = 6.4 \times 10^{-4}$ [26] with the distributions for $\bar{\nu}_e$ in energy and time shown as dashed lines in Fig. 1. The intrinsic $\bar{\nu}_e$ contamination is discussed in more detail in Sec. V B 3. The small $\bar{\nu}_e$ component in the ISIS ν beam together with the unique time structure of the proton beam allows a high sensitivity search for $\bar{\nu}_\mu \rightarrow \bar{\nu}_e$ oscillations.

B. The KARMEN detector

The KARMEN detector [27] is a segmented high resolution liquid scintillation calorimeter, located at a mean distance of 17.7 m from the ISIS target at an angle 100° relative to the proton beam. The liquid scintillator is enclosed by a multilayer active veto system and a 7000 t steel shielding (see Fig. 2). The hydrocarbon acts as active target for neutrino-nucleus reactions (^{12}C,^{13}C,^{1}H). The 65 m^3 of liquid scintillator consisted of a mixture of paraffin oil (75 % vol.), Pseudocumene (25 % vol.), and 2 g/l of the scintillating additive 1-phenyl-3-mesityl-2-pyrazoline (PMP).

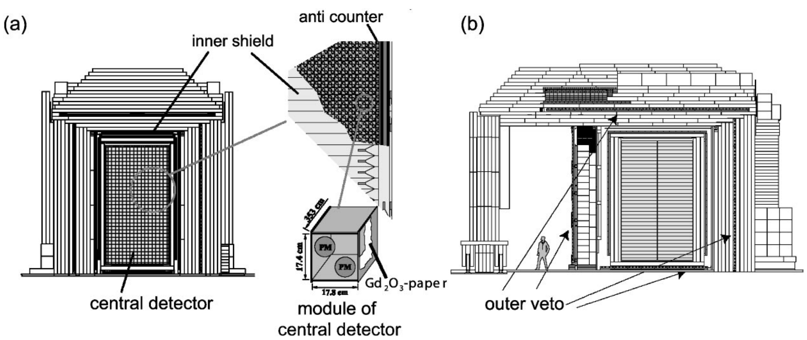

FIG. 2. (a) Front view of the KARMEN detector with details of the central detector region and a single module. (b) Side view, the ISIS target is located to the right.

The liquid scintillator volume is optically separated into independent modules by an optical segmentation of double lucite sheets. A small air gap between the double lucite sheets of the segmentation causes optical total reflection and thus a very efficient transport of scintillation light to the ends of the modules, where the scintillation light is read out by a pair of (3 inch VALVO XP 3462) photomultiplier tubes (PMT). Furthermore gadolinium coated paper has been put between the acrylic walls for an efficient detection of thermal neutrons.

The segmentation consisted of 608 modules in total, which are placed inside a rectangular tank with the dimensions of 3.53 m$\times$3.20 m$\times$5.96 m in length, width, and height. The central detector consists of the inner 512 modules (each with the dimensions of 353 cm$\times$17.7 cm $\times$18.1 cm in length, width, and height), arranged in 32 rows and 16 columns. A surrounding layer of modules with half the cross section of a central detector module defines the inner anti counter. An inner passive shielding of 18 cm thick steel slabs surrounds the scintillator tank providing passive shielding and mechanical stability. The second layer of active shielding (inner veto) consists of 136 plastic scintillator bars (NE110) with thicknes of 3 cm and lengths ranging from 2.4 m to 3.1 m, which are mounted onto the passive shielding on all sides but the bottom side.

The surrounding steel shielding is built in a modular way out of layers of steel slabs. This structure of layers allowed the integration of an outer veto system inside the steel shielding. In total, 136 bars of plastic scintillator (Bicron BC412) have been used for the outer veto system, which provided also active shielding under the detector.

This additional outer veto system was installed in 1996, marking the beginning of the KARMEN 2 experiment. The upgrade of the experimental configuration improved considerably the background level for the $\bar{\nu}_\mu \rightarrow \bar{\nu}_e$ search, as it will be outlined in Sec. V A.

The KARMEN detector is a liquid scintillator calorimeter, optimized for high energy resolution of $\sigma_E = 11.5\%/\sqrt{E(\mathrm{MeV})}$. An event information comprises the energy, time, and position information, as well as the number of addressed modules and their relative time differences. A scintillator module hit is accepted, if there is a coincidence of signals of the photomultipliers at both ends within a coincidence time of $\Delta T_{C1} = 190$ ns (first level trigger). The position of the event along the module axis (x direction) is obtained by the time difference between the signals. The position resolution is derived from calibration measurements and depends on the individual module as well as the position along the module axis. A typical electronlike event with an energy of 20 MeV in the middle of a module amounts to $\delta x = 7$ cm [full width at half maximum (FWHM)]. The energy information is derived from the integrated PMT pulses. The absolute energy calibration of the detector is fixed by the analysis of the Michel energy spectrum of electrons from stopped muon decay. The energy calibration is performed for each single module and takes into account the individual light output curves of the modules. Module hits within a coincidence time $\Delta T_C < 90$ ns are combined to one event. Analysis of throughgoing muons allow to calibrate theb relative times of module hits t_{rel} with an accuracy of $\delta t_{\mathrm{rel}} = 0.8$ ns (FWHM). In the case of events with more then one module hit, the 3-dimensional position information (x,y,z) corresponding to module axis, row, and column is constructed by the energy weighted average of the single module information. Finally, the event time t relative to the ISIS proton beam is recorded. Individual KARMEN modules are synchronized to the ISIS beam with an accuracy of $\delta t < 2$ ns, allowing one to exploit the ISIS time structure in detail. A beam reference time of $t = 0$ is attributed to the time, when the first neutrino enters the KARMEN detector. A full description of the detector energy and timing calibration is given in Ref. [28].

III. OSCILLATION SIGNATURE

Neutrino flavor oscillations occur if the weak interaction eigenstates ν_e, ν_μ, and ν_τ are a superposition of the nondegenerate mass eigenstates ν_1, ν_2, and ν_3. As the mass eigenstates propagate differently, there is a nonzero probability that a neutrino flavor produced via the weak interaction (e.g., $\bar{\nu}_\mu$) is detected as another neutrino flavor (e.g., $\bar{\nu}_e$) after a traveling distance L. In general, the formalism of the mixing of three flavor and mass eigenstates requires a unitary 3×3 mixing matrix U, often referred to as the Maki-Nakagawa-Sakata matrix U_{MNS} [29,30]. However, the current results in the field of neutrino oscillations suggest a one-mass-scale dominance $\delta m^2 \equiv \Delta m^2{}_{12} \ll \Delta m^2{}_{13}$ and $\Delta m^2{}_{13} \approx \Delta m^2{}_{23} \equiv \Delta m^2$ with $\Delta m^2{}_{ij} = |m_i^2 - m_j^2|; i,j = 1, \ldots, 3$ [31–37]. Possible mixing to sterile neutrinos as suggested by Ref. [13–15] is ignored whereas CP conservation is assumed, as we shall do in the following. In this case, and since the KARMEN experiment with its distance between neutrino source and detection point of $L \approx 17$ m is a typical short baseline oscillation experiment, it is sufficient to simplify the mixing scheme to a 2×2 mixing. In such a two flavor mixing scheme, the probability P to detect a $\overline{\nu}_e$ in an initially pure $\overline{\nu}_\mu$ beam with energy E (in MeV) after a path length L (in meters) can be described as

$$P(\overline{\nu}_\mu \rightarrow \overline{\nu}_e) = A \cdot \sin^2\left(\frac{1.27 \cdot \Delta m^2 \cdot L}{E}\right). \quad (1)$$

In a short baseline regime ($1/\Delta m^2 \approx L/E \ll 1/\delta m^2$), contributions to the oscillation probability P due to the smaller difference of the squared ν masses δm can be neglected. The oscillation amplitude A in Eq. (1) is a function of the elements of the mixing matrix U_{MNS}. For simplicity, we define

$$A = \sin^2(2\Theta) \quad (2)$$

keeping in mind that for a comparison of oscillation searches in a different mode than $\overline{\nu}_\mu \rightarrow \overline{\nu}_e$ appearance, one has to calculate A as the complete function of the 3×3 mixing matrix elements. For a review on neutrino masses and mixing and a complete formalism of neutrino oscillations see Ref. [38].

A. $\overline{\nu}_e$ absorption on protons

The appearance of $\overline{\nu}_e$ from $\overline{\nu}_\mu \rightarrow \overline{\nu}_e$ flavor oscillations is detected by the classical inverse beta-decay on the free protons of the scintillator

$$\bar{\nu}_e + p \longrightarrow n + (e^+) \qquad Q = -1.804\ \mathrm{MeV}$$

$$n_{therm} \rightarrow +\,{}^1\mathrm{H} \rightarrow {}^2\mathrm{H} + (\gamma)$$

$$n_{therm} \rightarrow +\mathrm{Gd} \rightarrow \mathrm{Gd} + n\,(\gamma) \quad \langle n \rangle = 3$$

The $\overline{\nu}_e$ signature is therefore a spatially correlated delayed coincidence between a prompt positron and a delayed γ event from a (n,γ) neutron capture reaction.

1. Positron signal

For different sets of parameters $\sin^2(2\Theta)$ and Δm^2 the oscillation probability $P(\overline{\nu}_\mu \rightarrow \overline{\nu}_e)$ is calculated varying $\overline{\nu}_\mu$ energies and flight paths. These $\overline{\nu}_e$ energy spectra are then transformed into positron spectra by means of the calculated energy dependence of the $p(\overline{\nu}_e,e^+)n$ cross section. The calculation used [39] takes into account weak magnetism and recoil effects, yielding a flux averaged cross section of $\sigma_{\mathrm{tot}} = 93.5\times 10^{-42}$ cm^2 for the $\overline{\nu}_\mu$ spectrum from μ^+ decay at rest. Because of the short baseline of $\langle L \rangle = 17.7$ m, the strongest $\overline{\nu}_\mu \rightarrow \overline{\nu}_e$ signal is expected at $\Delta m^2 = 2.8$ eV^2. Figure 3(a) shows the dependence of expected e^+ energy spectra for three mass difference values ($\Delta m^2 = 1,10,100$ eV^2), illustrating the modification of the energy spectrum due to oscillation effects. The spectra include experimental response functions such as energy and spatial resolutions, threshold efficiencies as well the integration of the oscillation probability over the detector volume. The visible energies of positrons extend up to 50 MeV with the oscillation signal mostly above 20 MeV. Figure 3(a) also demonstrates the power of

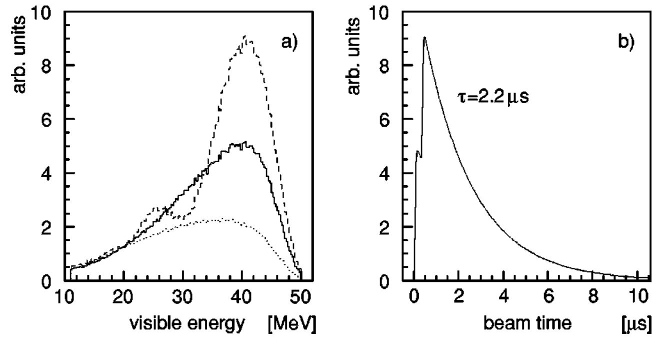

FIG. 3. Expected e^+ signal from $p(\overline{\nu}_e,e^+)n$. (a) Visible energy assuming $\Delta m^2 = 1$ eV^2 (dotted), 10 eV^2 (dashed), 100 eV^2 (solid) and (b) detection time.

the detector to discriminate between different values of Δm^2 in case of a positive oscillation signal.

Apart from the well defined energy spectrum, the time spectrum of e^+ [see Fig. 3(b)], resulting from the unique ISIS time structure, discriminates against beam uncorrelated background. The time distribution of the positrons follows the 2.2 μs exponential decrease of the μ^+ decay at rest. The positrons are therefore expected in a narrow time window of several μs after beam-on-target.

2. Neutron capture signal

The delayed event of the $\overline{\nu}_e$ induced delayed coincidence arises from one of two different neutron capture reactions. Neutrons from $p(\overline{\nu}_e,e^+)n$ reactions have kinematic energies up to 5 MeV and are quickly thermalized. After thermalization, neutrons are captured either on protons of the scintillator $p(n,\gamma)d$ or on gadolinium $Gd(n,\gamma)$, which is contained inside the walls of the segmentation. In the first case, a single monoenergetic 2.2 MeV gamma is produced, in the latter case, a complex gamma cascade is initiated with a sum energy of $\Sigma E_\gamma = 7.9$ MeV [40,41] [see Fig. 4(a)].

Neutron capture reactions are monitored *in situ* during the measurements by investigating the capture reaction

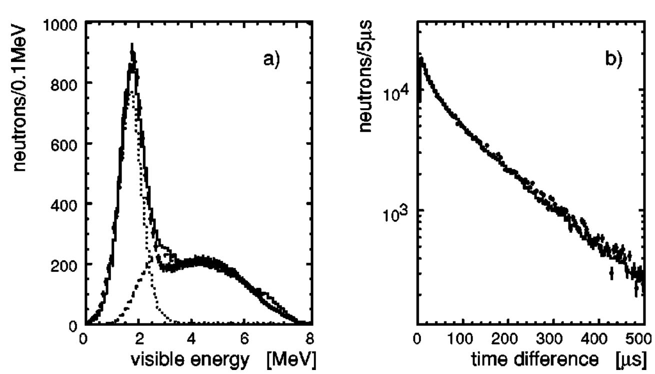

FIG. 4. (a) Energy and (b) time distribution of neutron capture events. The energy signal (experimental data points) is the sum of $p(n,\gamma)d$ (MC dotted line) and $Gd(n,\gamma)$ (MC dashed line) capture. The time between neutron production and capture is quasiexponential with a time constant of $\tau \approx 120$ μs well reproduced by MC.

$$\mu^- + {}^{12}\mathrm{C} \rightarrow {}^{12-x}\mathrm{B} + x \cdot n + \nu_\mu \qquad (3)$$

of stopped cosmic ray muons. This reaction produces neutrons with kinetic energies in the few MeV range [42], comparable to the energy of neutrons from the $p(\bar{\nu}_e,e^+)n$ process. Figure 4(a) shows the measured spectrum of visible energies following a stopped muon in a coincidence volume of $V_c \approx 1\ \mathrm{m}^3$ ($|\Delta x| < 60$ cm, $|\Delta\mathrm{row}|,|\Delta\mathrm{col}| \leq 2.5$) around the endpoint of the muon track. The $p(n,\gamma)d$ peak can be clearly separated from the broad distribution of $Gd(n,\gamma)$ signals. The $Gd(n,\gamma)$ signal does not peak at $E_0 = 7.9$ MeV due to the calorimetric properties of the single modules. If the γ's from the cascade are spread over different modules, missing visible energy can occur due to the thresholds of individual modules.

The neutron thermalization and capture followed by γ emission is simulated using the GEANT and GCALOR program [43,44]. The simulated spectra shown in Fig. 4(a) include detector response functions and have been adjusted separately to the measured distribution. For visible energies below 3–4 MeV the energy resolution, as well as hardware thresholds together with the complex topology of a multi-γ event lead to difficulties in describing the spectral shape by Monte Carlo simulations. However, since μ^- capture reactions [Eq. 3] are measured, the spectral shape of neutron capture events and the total neutron detection efficiency can be reliably measured, in order to be used for the $\bar{\nu}_\mu \rightarrow \bar{\nu}_e$ search.

The experimental as well as the MC generated time difference between the prompt cosmic muon and the γ's from the neutron capture is shown in Fig. 4(b). The distribution can be approximated by a single time constant of $\tau \approx 120\ \mu$s, reflecting the thermalization and diffusion processes of the neutron and the subsequent two competing capture processes. There is a slightly enhanced occurence of γ's within the first μs is due to a higher rate of $Gd(n,\gamma)$ capture. This is explained by the almost immediate capture of neutrons being produced near the walls containing Gd.

3. Neutron detection efficiency

The neutron detection efficiency ε_N has to be determined accurately in order to calculate the expected number of (e^+,n) sequences from $\bar{\nu}_\mu \rightarrow \bar{\nu}_e$ oscillations. The efficiency ε_N is determined by monitoring the nuclear capture reactions of stopped muons [Eq. 3]. It is given by the ratio of detected neutrons N_n to the total number of produced neutrons M_n.

The number of detected neutrons N_n is given by the number of delayed coincidences occuring after a stopped muon. According to the expected neutron capture signal, we require the delayed event to occur within a coincidence time $5 \leq \Delta t \leq 300\ \mu$s with energies $E_{\mathrm{del}} \leq 8$ MeV and within a coincidence volume of $V_c = 1.3\ \mathrm{m}^3$.

In order to derive the total number of produced neutrons M_n, the number N_{μ^-} of stopped μ^-, the μ^- capture rate Λ_c, and the neutron emission multiplicity $\langle x \rangle$ must be known. As the charge of stopped cosmic muons cannot be determined for individual tracks, the decay time spectrum has been analyzed to derive the charge ratio $\mu^+/\mu^- = R_\mu = 1.28 \pm 0.03$ and thus the number N_{μ^-} of stopped μ^- is known from the measured number of stopped muons N_μ. With a total μ^- capture rate of $\Lambda_c^{\mathrm{tot}} = (38.4 \pm 0.4) \times 10^{-3}\ \mathrm{s}^{-1}$ on ^{12}C [45] corrected for the abundance of ^{13}C and ^{16}O in the scintillator, an average probability per stopped μ^- of $\alpha_c^n = (64.1 \pm 1.3) \times 10^{-3}$ is derived for processes with neutron production.

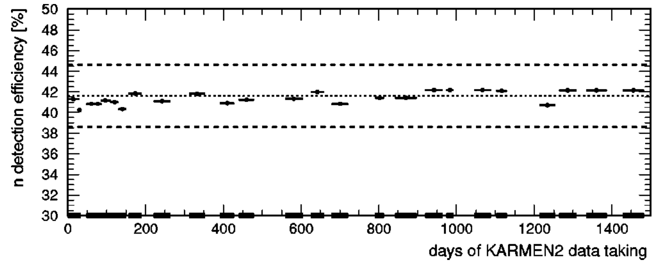

FIG. 5. Measured single neutron detection efficiency as a function of time during data taking. The horizontal bars indicate ISIS beam-on intervals, the dotted line shows the neutrino-flux weighted average of the neutron detection efficiency, the dashed lines the total systematic error band.

The derived neutron detection efficiency $\tilde{\varepsilon}$ from these values

$$\tilde{\varepsilon} = \frac{N_n \cdot (1 + R_\mu)}{N_\mu \cdot \alpha_c^n} \qquad (4)$$

must then be modified in two aspects:

(1) Due to multiple neutron emission $\langle x \rangle = 1.07$ [see Eq. (3)], the derived efficiency $\tilde{\varepsilon}$ must be corrected to the single neutron expectation from the $p(\bar{\nu}_e,e^+)n$ reaction.

(2) As the identification of the muon stop point can lead to ambiguities for tracks, which stop close to the borders of the detector, a restricted fiducial volume of the detector to the stop points of muons ($|x_{\mathrm{stop}}| < 150$ cm, the outermost module layer removed) is applied. The detection efficiency $\tilde{\varepsilon}$ is then extrapolated to the entire detector volume using GEANT or GCALOR simulations.

A complete description of the analysis of muon capture reactions with the KARMEN detector and the derivation of the neutron detection efficiency is given in Ref. [46]. Taking all effects into account, the neutron detection efficiency ε_N amounts to

$$\varepsilon_N = 0.42 \pm 0.03. \qquad (5)$$

This value is the neutrino flux weighted average of the entire KARMEN 2 measuring period as shown in Fig. 5.

B. $\bar{\nu}_e$ absorption on carbon

A second $\bar{\nu}_e$ detection reaction is the inverse beta decay of carbon ${}^{12}\mathrm{C}(\bar{\nu}_e,e^+n){}^{11}\mathrm{B}$ with a Q value of 16.7 MeV. This $\bar{\nu}_e$ detection reaction has a smaller flux-averaged cross section [47] than $p(\bar{\nu}_e,e^+)n$. In addition, the number of target atoms N_T in the scintillator is smaller than the number of free

TABLE I. Comparison of flux averaged cross sections σ and target nuclei N_T for detection of $\bar{\nu}_e$ from different sources.

	$p(\bar{\nu}_e,e^+)n$	$^{12}C(\bar{\nu}_e,e^+n)^{11}B$
N_T	4.5×10^{30}	2.5×10^{30}
$\sigma(\bar{\nu}_\mu\rightarrow\bar{\nu}_e)$	93.5×10^{-42} cm^2	8.5×10^{-42} cm^2
$\sigma(\bar{\nu}_e$ contamination)	72.0×10^{-42} cm^2	7.4×10^{-42} cm^2

protons (see Table I). It thus contributes about 5% to the detection of $\bar{\nu}_e$. The GEANT3.21 Monte Carlo simulation of $^{12}C(\bar{\nu}_e,e^+n)^{11}B$ is included in the total number and spectral shape of expected (e^+,n) sequences from $\bar{\nu}_\mu\rightarrow\bar{\nu}_e$ oscillations [Fig. 3(a)].

IV. GENERAL EVENT REQUIREMENTS

The special feature of the $\bar{\nu}_\mu\rightarrow\bar{\nu}_e$ signature is its delayed coincidence nature of a prompt high energetic positron, followed by a low energetic signal from neutron capture. Before enforcing stringent cuts, which correspond to the delayed coincidence nature of the $\bar{\nu}_e$ detection reaction, we apply loose cuts to the data set, which do not cut into the signal region but which strongly suppress background.

(1) Only sequences of two events are accepted.

(2) A sequence accepted for further evaluation in the software analysis consists of a prompt event and a delayed event, which shows the typical characteristics of neutron capture events. In particular, this means that the delayed signal occurs within $\Delta t<500$ μs after the prompt event and has energies less than $E_{\rm del}<8$ MeV. A coincidence volume of $V_c=1.3$ m^3 is required.

(3) Neither the prompt event nor the delayed event must have any hits in the multilayer veto system.

(4) The prompt event must have energy $E_{\rm pr}>11$ MeV.

(5) There must be no activity in the detector system preceding a prompt event. The history of all activities in the detector system (total trigger rate $\Gamma_{\rm tot}\sim13$ kHz) are stored by a time stamp and a bit pattern word, which allows the decryption of addressed detector parts. Requesting no activities preceding an event in the main detector, inner veto or inner anticounter in the previous 24 μs (14 μs for the outer veto system) eliminates most of the cosmic induced background with short time correlations, as shown in Fig 6.

(6) There must be no stopped muons in the central detector preceding a prompt event. With a rate of $\Gamma_\mu\sim160$ Hz the hardware trigger identifies stopped muon in the central detector. A 10 μs hardware dead time is then applied and the event time and stopping position of the muon are stored, thus providing information for the offline analysis to detect spatial correlations between an event and preceding stopped muons. Prompt events of a potential $\bar{\nu}_e$ coincidence are rejected, if they occur within $\Delta t<40$ μs after stopped muons anywhere in the central detector, after up to $\Delta t<500$ μs within a coincidence volume of $V_C=1.3$ m^3 (μ^- capture with n emission), or if they occur in a coincidence volume of $V_C=0.5$ m^3 for time differences $\Delta t<100$ ms (μ^- capture with subsequent ^{12}B β decay).

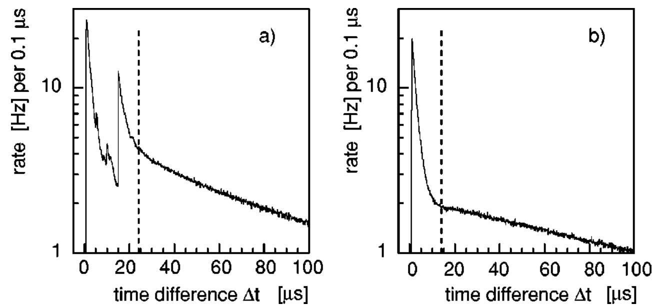

FIG. 6. Rate of events following in a time difference Δt to the last preceding event (a) in the main detector, inner veto or anticounter and (b) in the outer veto system. The count rate suppression for time differences $\Delta t<15$ μs in (a) is caused by hardware and software deadtimes as well as read-out dead times.

(7) In the case of events with more than one addressed module in the central detector, the maximum time difference between the module hits must not exceed $\Delta T_{\rm cmod}=50$ ns, ensuring that the module hits belong to the same physical event.

(8) Not more than 10 modules of the central detector must be addressed.

V. BACKGROUND REACTIONS

Evidence for flavor oscillations $\bar{\nu}_\mu\rightarrow\bar{\nu}_e$ in the appearance mode requires statistically significant detection of $\bar{\nu}_e$ in the time window of $\bar{\nu}_\mu$ in excess of any inherent background. While for maximal mixing one expects several thousands of oscillation events, a mixing amplitude $10^{-3}<A<10^{-1}$ (as suggested by LSND) could reduce this number to about 10 events. Despite the clear oscillation signal and the small ISIS duty cycle, the clear and unambiguous detection of such rare $\bar{\nu}_e$ events requires a very efficient detection and suppression of the large amount of cosmic induced reactions. Benefiting from the threefold active veto system the cosmic background can be suppressed to a level well below the expected oscillation events.

However, neutrino induced reactions can also induce a background rate. In particular, ν_e induced charged and neutral current reactions constitute the largest background reactions in the search for $\bar{\nu}_\mu\rightarrow\bar{\nu}_e$ oscillations. This section discusses both background reactions in the $\bar{\nu}_e$ search, induced by cosmic rays as well as by neutrinos.

A. Cosmic induced background

The cosmic ray induced background reactions are measured in the long beam–off time window between the ν pulses. Taking into account the trigger structure of the experiment, which also allows for calibration measurements, the effective statistics for cosmic induced reactions in the beam-off time interval is 140 times larger than the narrow time interval for the ν pulse. This factor allows one to extrapolate the determined cosmic induced background rate with a statistical accuracy of 5% of the neutrino analysis.

The 7000 t steel shielding of the detector absorbs both the hadronic and electromagnetic component of cosmic rays. It is therefore only the muonic component, which can induce $\bar{\nu}_e$-like background processes.

1. Throughgoing muons

The KARMEN central detector was exposed to a rate of 1.1 kHz of throughgoing muons. These muons were detected in the central detector modules, as well as by the active veto system. The veto system inefficiency is estimated to be less than 2.2×10^{-5}. Delayed activities following cosmic ray muons by spallation processes of high energetic muons on ^{12}C, are highly suppressed due to the general event requirement 5 (see Sec. IV) and can be neglected in the $\bar{\nu}_e$ search.

2. Stopped muons

Stopped muons in the central detector can cause spatially correlated events on the time scale of a few microseconds up to several milliseconds. Whereas all μ^+ stopping in the detector will decay, a fraction of $\alpha_c=7.8\%$ of the stopped μ^- undergo nuclear capture reactions in the scintillator. The muon decay produces a spatially correlated electron or positron with an energy up to $E_0=52.8$ MeV. The time correlation is defined by the lifetime of μ^+ ($\tau=2.197$ μs) and μ^- ($\tau=2.026$ μs). With a branching ratio of $\Gamma_{\mu^-}=0.82$, the nuclear capture reactions involve neutron production:

$$\mu^- + {}^{12}\mathrm{C}\rightarrow {}^{12-x}\mathrm{B}+x\cdot n+\nu_\mu. \tag{6}$$

The neutrons are detected by the typical neutron capture events of $p(n,\gamma)$ or $Gd(n,\gamma)$ with $E_0=8$ MeV and $\tau_{\mathrm{capture}}\approx120$ μs. This process leads to a contribution to the cosmic induced background in the $\bar{\nu}_e$ search, which arises from unvetoed muons with short track lengths, stopping in the central detector and depositing less than 51 MeV.

Long lived background arises from muon capture reactions of μ^-

$$\mu^- + {}^{12}\mathrm{C}\rightarrow {}^{12}\mathrm{B}+\nu_\mu \tag{7}$$

to the ^{12}B ground state or γ-unstable levels, through the subsequent β decay.

$${}^{12}\mathrm{B}_{\mathrm{g.s.}}\rightarrow {}^{12}\mathrm{C}+e^- +\bar{\nu}_e \tag{8}$$

with $\tau=29.1$ ms and an end point energy of $E_0=13.3$ MeV for the beta-electron. Hence, this reaction has only a small overlap in its signature to $\bar{\nu}_e$ induced coincidences. Nevertheless, each event arising in the main detector is checked for preceding stopped muons for time differences up to $\Delta t<100$ ms (general event requirement No. 6) to suppress the beta decay, whose electrons otherwise give rise to random coincidences.

3. Muons near the central detector

The dominant cosmic ray induced background is due to muon interactions in the 7000 t steel shielding blockhouse, which generate highly energetic neutrons. Two different reaction mechanisms can be distinguished

μ^- capture on ^{56}Fe:

$$\mu^- + {}^{56}\mathrm{Fe}\rightarrow {}^{56-x}\mathrm{Mn}+x\cdot n+\nu_\mu. \tag{9}$$

Negative charged muons stopped in iron are predominantly captured with a capture rate of $\lambda_c=(4.411\pm0.026)\times10^6/s$ [48]. The energy transferred to the nucleus in the process is between 15 and 20 MeV and therefore above the neutron emission threshold.

Deep inelastic scattering (DIS) of muons on ^{56}Fe :

$$\mu^\pm + {}^{56}\mathrm{Fe}\rightarrow \mathrm{X}+y\cdot n+\mu^\pm. \tag{10}$$

Virtual photons radiated from the cosmic muons interact with the iron nuclei and can produce spallation neutrons with energies up to a few GeV. On average, 3–4 secondary particles with energies above 10 MeV are produced, primarily neutrons and protons. Neutrons from deep inelastic scattering can penetrate into the liquid scintillator, causing signals with visible energies up to 200 MeV through elastic n-p scattering. After thermalization the neutrons are captured either on protons or on the gadolinium, yielding capture γ spectra, as shown in Fig. 4. Thus, the highly energetic neutrons cause delayed coincidences, which are nearly identical to the signature of $\bar{\nu}_e$, as the KARMEN detector has no particle identification and cannot distinguish between cosmic induced n-p recoil events and positrons from $p(\bar{\nu}_e,e^+)n$. The crucial identification of the highly energetic neutrons is achieved by the third veto counter system, which is placed inside the steel shielding. Figure 7 shows the spectrum of the visible energies of the prompt events, covering the entire energy interval of a potential oscillation signal. The delayed events of these sequences follow the expected distributions for neutron capture (see Fig. 4).

Figure 8 shows the identification of the processes involved by the time correlation of prompt muons and the proton recoil event. The time distribution is measured by the time difference δt between the hit in the outer veto system caused by the muon and the subsequent hit in the central detector caused by the proton recoil from highly energetic neutron interaction. The time distribution shows three components.

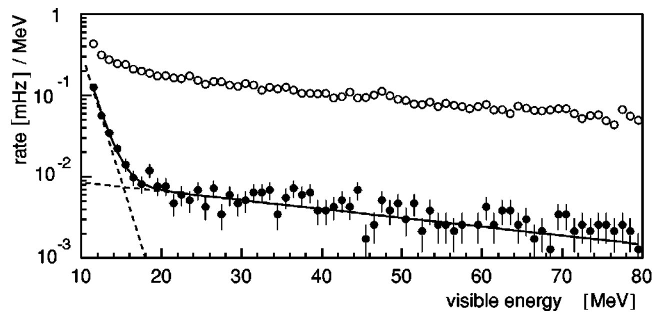

FIG. 7. Energy distribution of prompt events of cosmic induced sequences. Measurement ignoring information (open dots) and using information (full dots) of the outer veto system. See text for details on the exponential fits.

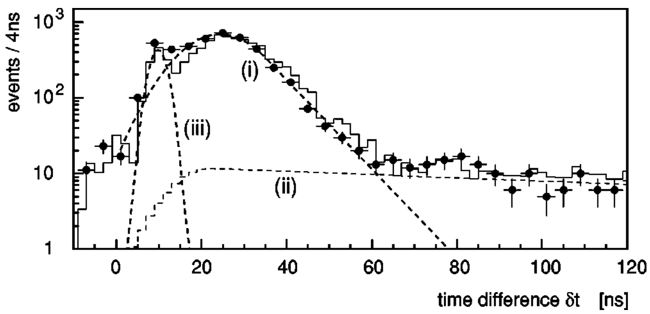

FIG. 8. Distribution of time difference δt between hits in the outer veto and subsequent hits in the central detector of cosmic induced background. The Monte Carlo simulation (solid line) consists of three components: (i) fast neutrons from DIS, (ii) neutrons from muon capture on iron, (iii) stopped muons.

(i) The dominant Gaussian shaped distribution peaking at a time difference of $\delta t = 25$ ns with an additional enhanced tail distribution, which can be attributed to highly energetic neutrons from deep inelastic muon scattering on iron. The time difference for these events is equivalent to the time of flight of the neutrons from their point of production in the steel shielding to their n–p interaction in the central detector.

(ii) For time differences $\delta t > 60$ ns neutrons from μ^- stopping in iron with subsequent nuclear capture $^{56}\mathrm{Fe}(\mu^-,n)^{55}\mathrm{Mn}$ dominate. The time correlation of these neutrons largely reflects the capture rate of muons in iron ($\tau = 206$ ns) [48].

(iii) In the time interval $0 < \delta t < 20$ ns there is an additional component, caused by muons which hit the outer veto and stop within the central detector. In this case, the time distribution corresponds to the muon time of flight from the veto to the central detector.

The solid histogram in Fig. 8 represents the expected time distribution from GEANT3.21 simulations, which are in good agreement with the experimental data and are described in detail in Ref. [49].

Having identified events induced by cosmic ray interactions on iron using the outer veto, this background is strongly suppressed. The measurement indicated by full circles in Fig. 7 shows the remaining cosmic induced background, if sequences are rejected where the prompt events have simultaneously addressed modules in the central detector and in the outer veto system. These remaining sequences constitute the cosmic ray induced background for the $\bar{\nu}_e$ analysis. They arise from the fraction of neutrons, which are produced outside the outer veto system, and are not absorbed in iron on their path to the detector (attenuation length of highly energetic neutrons in iron $\Lambda = 21.6$ cm [50]). The remaining spectrum consists of two components. The soft component is caused by neutrons from muon capture reactions and can be described as an exponential distribution e^{-E/E_0} with $E_0 \approx 1.4$ MeV. The much harder component is attributed to neutrons, which have been produced in deep inelastic scattering processes of cosmic ray muons. This second component with a parameter of $E_0 \approx 42$ MeV covers the entire region of interest for the oscillation search.

Compared to the background rates before the installation of the outer veto system (corresponding to the energy spectrum with open circles in Fig. 7), a background suppression by a factor 35 is achieved, resulting in a total rate of $R_{CB} = (0.20 \pm 0.01)$ mHz for the data cuts of the $\bar{\nu}_\mu \to \bar{\nu}_e$ analysis in Sec. VI. With this rate the cosmic induced background is smaller than the neutrino induced background.

B. Neutrino induced background

A second source of background reactions arises from the charged current (CC) and neutral current (NC) interactions of ν_e and $\bar{\nu}_\mu$ with the carbon nuclei of the liquid scintillator and iron nuclei of the inner passive shielding. To estimate the background contributions arising from different CC and NC reaction channels, the experiment takes advantage of having measured all relevant cross sections in a series of precision measurements [18,19]. Thus, the calculated number of background events from conventional neutrino interactions does not rely on theoretical estimates of neutrino induced cross sections. This is especially important, as the ν-induced background is the dominant background contribution to the KARMEN neutrino oscillation search.

In the following we discuss the different ν-induced background reactions in detail. For each background component we specify the experimental cross section as well as the detailed spectral information on energy and time, which have been used to calculate its contribution to the $\bar{\nu}_\mu \to \bar{\nu}_e$ oscillation search.

1. The ν_e induced charged current reaction

Exclusive charged current interactions of ν_e with ^{12}C can be detected by a delayed coincidence consisting of a prompt electron from the inverse beta reaction $^{12}\mathrm{C}(\nu_e,e^-)^{12}\mathrm{N}_{\mathrm{g.s.}}$ and the subsequent detection of a delayed positron from $^{12}\mathrm{N}_{\mathrm{g.s}}$ decays

$$\nu_e + {}^{12}\mathrm{C} \longrightarrow {}^{12}\mathrm{N}_{\mathrm{g.s.}} + \text{ⓔ}^- $$
$$\hookrightarrow {}^{12}\mathrm{C} + \text{ⓔ}^+ + \nu_e$$

The lifetime of $^{12}\mathrm{N}_{\mathrm{g.s}}$ is $\tau = 15.9$ ms and the β-decay end point amounts to $E_0 = 16.3$ MeV. In total, 860 sequences of this type have been identified with a signal to background ratio of 61:1. Figure 9 shows the spectral information of the measured sequences, which are both for the prompt events and the delayed events in good agreement with the expectation from simulation. This fact underlines the reliability of the use of these simulated spectra in the likelihood analysis later applied. The measurements of KARMEN 1 and KARMEN 2 show full compatibility. For definiteness we use in the following the published CC event sample of KARMEN 1 [25], which leads to a cross section of

$$\sigma = [9.4 \pm 0.4(\mathrm{stat.}) \pm 0.8(\mathrm{sys.})] \times 10^{-42}\ \mathrm{cm}^2. \qquad (11)$$

It is the small fraction of 1.7% of $^{12}\mathrm{N}_{\mathrm{g.s}}$ decaying within the first 300 μs and depositing visible energies of less than 8 MeV which contribute to the expected background in the $\bar{\nu}_e$

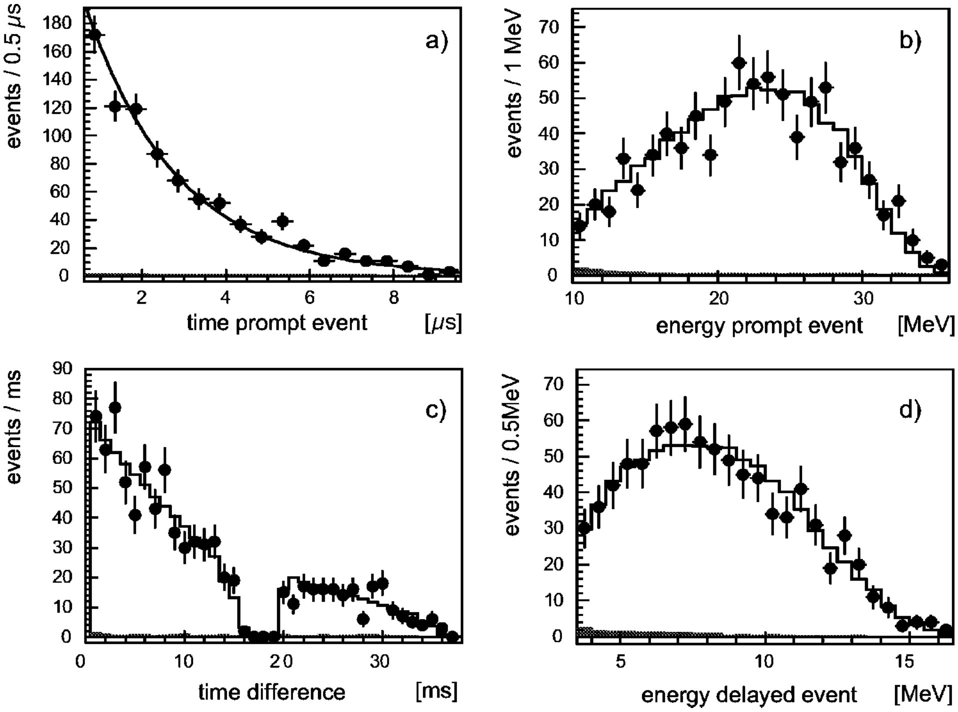

FIG. 9. (a) Measurement of $^{12}C(\nu_e,e^-)^{12}N_{g.s.}$ reactions (measuring points), leading to long lived coincidences between prompt e^- and delayed e^+ from $^{12}N_{g.s}$ decay [solid line (MC), shaded area (background)]. (a) Event time of e^-, (b) visible energy of e^-, (c) time difference between e^- and e^+, (d) visible energy of e^+. The deviation from a pure $\tau=15.9$ ms exponential decay curve in (c) is caused by hardware dead times at the end of a beam period and data acquisition read-out times (16–20 ms).

search. This background is extrapolated from the measured number of charged current sequences with time differences of $0.5<\Delta t<35.5$ ms to the smaller time interval $0.5<\Delta t<300$ μs on basis of the known $^{12}N_{g.s}$ lifetime and the $^{12}N_{g.s}$ energy spectrum. The uncertainties in the extrapolation correspond to 5% accuracy in the prediction of this background component.

Charged current reactions of ν_e on iron with subsequent neutron evaporation from the excited iron nucleus $^{56}Fe(\nu_e,e^-n)^{56}Co$ have been investigated and simulated as possible background channel. Despite the rather high cross section calculation of $\sigma=34.8\times10^{-42}$ cm^2 for this reaction channel [51] and the significant number of target nuclei of the inner passive shielding $N_T=2.4\times10^{30}$, ν_e reactions on iron do not give rise to background in the $\bar{\nu}_\mu\rightarrow\bar{\nu}_e$ analysis. The suppression of this channel is caused by the low efficiency of the electrons, which are produced with energies up to 35 MeV inside the steel, to be detected in coincidence with the neutron events inside the central detector.

2. Random coincidences

Neutrino-nucleus interactions as well as neutrino electron scattering increases the number of events in the positron time window in the first few μs after beam on target. This implies an enhanced rate of random coincidences between a neutrino induced (prompt) event and a low energy event from environment activity. Random coincidences, initiated by cosmic induced events, are accounted for in the measurement of the cosmic induced background. The probability P_{rc} of an un-search criteria to uncorrelated events, for example, to events recorded in preceding beam periods. This method allows one to determine P_{rc} and the spectral information of the delayed events with high statistics.

In the energy range from $11<E<50$ MeV and in the time window $0.6<t<10.6$ μs after beam on target, 1567 neutrino-nucleus interactions are measured. The neutrino interactions arise mainly from two different types of neutrino-nucleus interactions. The largest contribution arises from the inclusive charged current reaction $^{12}C(\nu_e,e^-)^{12}N$, as well as from neutral current reaction $^{12}C(\nu,\nu')^{12}C^*(1^+,1;15.1\text{ MeV})$ with $\nu=(\nu_e,\bar{\nu}_\mu)$. The neutral and charged current contribution are clearly visible in the energy spectrum of the measured neutrino-nucleus interactions (see Fig. 10). The delayed events of random coincidences are uniformly distributed in time, and their energies are close to the threshold of a single detector module (mean energy $\langle E\rangle=1.1$ MeV) as shown in Fig. 10(b).

The probability P_{rc} for an uncorrelated event to occur with a time difference of up to $5<\Delta t<300$ μs and within a coincidence volume of $V_c=1.3$ m^3 after the prompt event is

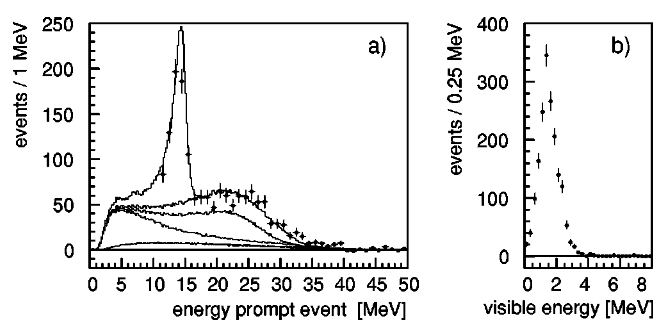

FIG. 10. (a) Measurement of neutrino induced reactions in the time window $0.6<t<10.6$ μs. The calculated contributions are (bottom to top): $\nu-e^-$ scattering, $^{56}Fe(\nu_e,e^-)^{56}Co$, $^{12}C(\nu_e,e^-)^{12}N^*$, $^{12}C(\nu_e,e^-)^{12}N_{g.s.}$, and $^{12}C(\nu,\nu')^{12}C^*$. (b) Energy distribution of uncorrelated delayed events.

determined to be $P_{rc}=(5.5\pm 0.4)\times 10^{-3}$ [52]. The expectation value for the neutrino-induced random background N_{rc} is obtained by multiplying the number of measured neutrino-induced reactions N_{ν} with the probability P_{rc}. Using this method, the statistical accuracy of N_{rc} is 7%. The measured spectral information is used for the likelihood analysis.

3. $\bar{\nu}_e$ contamination

The only background source, which cannot be directly extracted from the data, is the contamination of the neutrino beam with $\bar{\nu}_e$ produced in the π^--μ^- decay chain. Detailed Monte Carlo simulations, including a three-dimensional model of the ISIS target, and its surroundings are used to obtain the fraction of π^- and μ^- decaying before they undergo capture on nuclei of the target materials [53,26]. The overall ratio of $\bar{\nu}_e$ produced in the ISIS target relative to $\bar{\nu}_\mu$ from μ^+ decay amounts to $\varepsilon=6.4\times 10^{-4}$. This ratio is further reduced by taking into account, that the lifetime of μ^- depends on the target material and is in general shorter than the μ^+ decay time (see Fig. 1), leading to a further reduction of $\bar{\nu}_e$ by a factor of 0.764 in the time window of $0.6<t<10.6$ μs. Finally, the $\bar{\nu}_e$ spectrum from μ^- decay [Fig. 1(b)] leads to a lower flux averaged cross section of $\sigma=72.0\times 10^{-42}$ cm^2 for the $p(\bar{\nu}_e,e^+)n$ reaction (see Table I). Taking all effects into account, the intrinsic $\bar{\nu}_e$ contamination leads to the smallest background contribution in the $\bar{\nu}_e$ search.

C. Beam correlated neutron background

Each 800 MeV protons of the ISIS beam produces typically 25 spallation neutrons in the target with energies up to 400 MeV [54]. The 7 m steel shielding between ISIS target and detector reduces the neutron flux by a factor of more than 10^{15}. Despite the flux reduction, punch-through neutrons are observed in the central detector. However, these high energy neutrons closely follow the ISIS double proton pulses [20] and are restricted to the time window of $t<500$ ns after beam on target. Setting the lower time cut for the positron window at $t_{\mathrm{pr}}>600$ ns after beam on target, completely eliminates reactions from these neutrons.

VI. DATA REDUCTION

A. Raw data

The results presented here are based on measurements from February 1997 to March 2001. During this time, protons equivalent to an accumulated total charge of 9425 Coulombs have been stopped in the ISIS target. This corresponds to a total number of

$$N_{\nu}=2.71\times 10^{21} \tag{12}$$

neutrinos for each of the flavors ν_e, $\bar{\nu}_\mu$, and ν_μ produced at the ISIS beam stop.

In total, the KARMEN data acquisition system recorded 3.7×10^9 events. Out of these single events, 1.93×10^7 have no hits in the veto counter system and deposit more than 11 MeV and hence can be classified as candidates for a prompt event of a delayed coincidence. Requiring in addition the detection of a second event without veto hits in the following 500 μs results in 3.5×10^5 delayed coincidences. After application of the general event requirements, defined in Sec. IV, the sample size shrinks to 3464 coincidences with more than 99% of these coincidences outside the time window of the $\bar{\nu}_\mu\to\bar{\nu}_e$ analysis.

The detector system was 777.4 days online, excluding additional measurements for specific background studies and calibration purposes. Taking into account ISIS beam on times, the duty cycle, and a 10 μs long neutrino time window, the effective neutrino measuring time amounts to 7.5 h.

B. Final selection criteria

The final selection criteria have been evaluated in order to optimize the sensitivity of the experiment. Since the true values of the oscillation parameters are unknown, we optimized the data reduction to deliver the most stringent upper limit on $\sin^2(2\Theta)$ for a given Δm^2 under the assumption that there are no $\bar{\nu}_\mu\to\bar{\nu}_e$ oscillations. Even a small oscillation signal would then first materialize as a much less stringent upper limit than the experimental sensitivity. The optimized cuts were obtained by simulating and analyzing experimental outcomes with different cuts leading to different event statistics [49]. It turned out that the achievable sensitivity only slightly depends on the variation of reasonable data cuts.

The final data cuts are as follows: Accounting for the ISIS time structure, the e^+ from $\bar{\nu}_\mu\to\bar{\nu}_e$ oscillations must be detected in the time interval of $0.6<t_{\mathrm{pr}}<10.6$ μs after beam on target, in which 84.0% of all $\bar{\nu}_\mu$ are expected. The lower time cut of 600 ns is chosen to eliminate any contributions from beam correlated fast neutrons (see Sec. V C). The lower cut on the visible energy deposit E_{pr} of a positron candidate is 16 MeV. This energy cut eliminates the neutral current contributions $^{12}\mathrm{C}(\nu,\nu')^{12}\mathrm{C}^*$ to the neutrino induced random background (Fig. 10) and also suppresses the soft component of the cosmic induced background (Fig. 7). No fiducial volume cut for the e^+ is applied.

The time difference for the delayed neutron capture event is restricted to the interval $5<\Delta t<300$ μs. Here, the lower time cut is fixed by a minimum hardware deadtime after the electronic read-out of the prompt event. The upper time cut at $\Delta t<300$ μs is an outcome of the MC procedure mentioned previously and reflects the different time distributions of delayed events from neutron capture ($\tau\approx 120$ μs) and from the background reactions of random coincidences (uniformly distributed) and charged current coincidences ($\tau=15.9$ ms).

The remaining data cuts for neutron capture events are the coincidence volume of $V_c=1.3$ m^3 and a maximum energy of the neutron capture event of $E_{\mathrm{del}}<8.0$ MeV. Table II gives a summary of the applied data cuts and the corresponding efficiencies ε, resulting in a total efficiency

TABLE II. Final data cuts and efficiencies for the $\overline{\nu}_\mu \rightarrow \overline{\nu}_e$ search. The efficiency for the energy cut corresponds to oscillation parameters $\Delta m^2 \geqslant 100$ eV^2.

event	data cut	efficiency ε
	check on previous history, (see sec. IV)	0.709
e^+	$0.6\ \mu s < t_{pr} < 10.6\ \mu s$	0.840
	$16\ \mathrm{MeV} < E_{pr} < 50\ \mathrm{MeV}$	0.775
(n,γ)	$5\ \mu s < \Delta t < 300\ \mu s$ $E_{del} < 8.0\ \mathrm{MeV}$ $V_c = 1.3\ \mathrm{m}^3$	0.416

$$\varepsilon_{tot}(\overline{\nu}_e) = 0.192 \pm 0.0145 \qquad (13)$$

for an oscillation signal at large Δm^2.

C. Data reduction

Applying the final selection criteria to the entire KARMEN 2 data set results in 15 $\overline{\nu}_e$ candidate events. The total background expectation amounts to $N_{BG}^{exp} = (15.8 \pm 0.5)$ events for the components described in Sec. V. As can be seen from the summarizing Table III, the background is dominated by neutrino induced processes, whereas the cosmic induced background contributes to only 25% of the total rate. The relative uncertainty of the background expectation amounts to 5%, reflecting the accuracy of the *in situ* measurement of the three dominating background components in different energy and time windows. Figure 11 shows the spectral distribution of the 15 candidate events with the superimposed background expectation, normalized to 15.8 events. In each plot the measured data agree well with the expected background distributions. There are no obvious deviations from the background expectations, neither for the prompt nor delayed events.

Already, the agreement of the number for measured events with the expected background does not give any hint for an oscillation signal within the KARMEN 2 data. In the following, we will set upper limits on the oscillation parameters, also using spectral information of the candidate events.

VII. DATA ANALYSIS

For $\overline{\nu}_\mu \rightarrow \overline{\nu}_e$ oscillations with maximal mixing $[\sin^2(2\Theta) = 1]$ and large mass differences ($\Delta m^2 \geqslant 100$ eV^2), an oscillation signal of (2913 ± 269) sequences is expected (see Table IV). This number includes a small contribution from $\overline{\nu}_\mu$ produced at the intermediate ISIS μSR target [55]. The systematic error of the oscillation expectation is dominated by the neutrino flux uncertainty of 6.5% [53] and the error in the determination of the neutron detection efficiency of 7.0%.

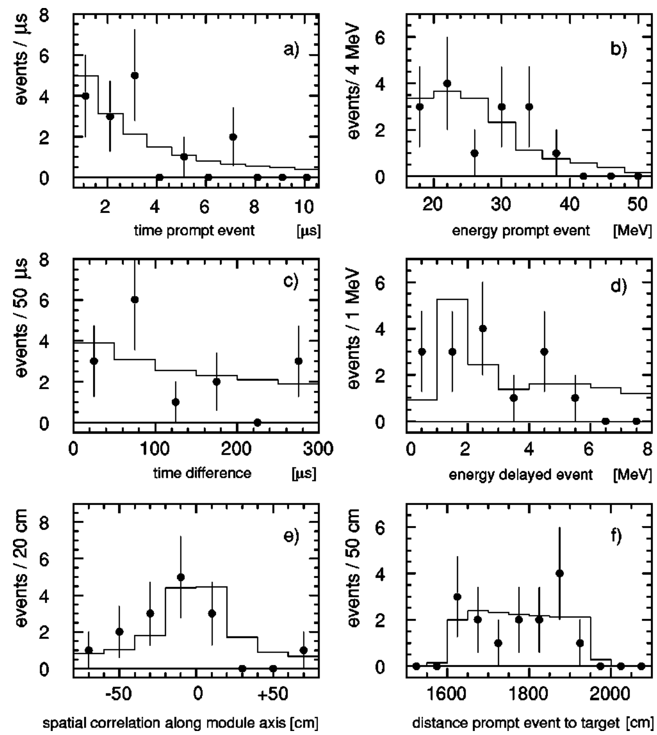

FIG. 11. Final event ensemble (a) time of prompt events, (b) energy of prompt events, (c) time difference between prompt and delayed event, (d) energy of delayed events, (e) spatial correlation, and (f) distance to target of prompt event. The 15 oscillation candidates are in very good agreement with the background expectation of 15.8 events (solid line).

Having measured 15 events with a background expectation of 15.8 events, there is no indication for the presence of an oscillation signal in the KARMEN data. Ignoring, in a first step, the spectroscopic information of the measurement and interpreting the experimental outcome as a pure counting experiment, an oscillation signal larger than $N_{sig} = 7.4$ events is excluded in 90% confidence interval (C.I.) [56,57]. However, such a simplified approach does not make any use of the spectroscopic quality of the data. In order to extract more information on a potentially small oscillation signal in the

TABLE III. Expected background contributions.

background	expectation N_i	method of determination
Cosmic induced background	3.9 ± 0.2	measured in diff. time window
Charged current coincidences	5.1 ± 0.2	measured in diff. energy, time windows
ν_e ind. random coincidences	4.8 ± 0.3	measured in diff. time window
$\overline{\nu}_e$ contamination	2.0 ± 0.2	MC simulation
Total background N_{BG}^{exp}	15.8 ± 0.5	

TABLE IV. Expected $\overline{\nu}_\mu \to \overline{\nu}_e$ oscillation signal for maximal mixing.

detection reaction	expectation N_{sig}	neutrino source
$p(\overline{\nu}_e, e^+)n$	2716 ± 268	$\overline{\nu}_\mu \to \overline{\nu}_e$ from main target
$p(\overline{\nu}_e, e^+)n$	73 ± 7	$\overline{\nu}_\mu \to \overline{\nu}_e$ from μSR target
$^{12}\mathrm{C}(\overline{\nu}_e, e^+ n)^{11}\mathrm{B}$	125 ± 17	$\overline{\nu}_\mu \to \overline{\nu}_e$ from main target
Total $N_{\mathrm{sig}}^{\mathrm{exp}}[\sin^2(2\Theta)=1, \Delta m^2 = 100\ \mathrm{eV}^2]$	2913 ± 269	

final event ensemble, a single event based maximum likelihood analysis is applied to this ensemble.

A. Likelihood analysis

The purpose of a maximum likelihood analysis is the separation of a potential signal from background by maximizing the likelihood function with regard to some unknown parameters. In this case, the signal corresponds to (e^+, n) sequences from $\overline{\nu}_\mu \to \overline{\nu}_e$ oscillations, the unknown estimators are the oscillation parameters $\sin^2(2\Theta)$ and Δm^2 . The likelihood function $\tilde{\mathcal{L}}$ is defined as

$$\tilde{\mathcal{L}}(r, \Delta m^2) = \prod_{n=1}^{N_{\mathrm{sample}}} [r \cdot f_{\mathrm{sig}}(\vec{x}_n, \Delta m^2) + (1-r) \cdot f_{\mathrm{bg}}(\vec{x}_n)] \tag{14}$$

with the following definitions.

The event sample with $N_{\mathrm{sample}} = 15$ candidate events is characterized by the information on the energy E_{pr} and time T_{pr} of the prompt event, the energy of the delayed event E_{del} and the time difference ΔT and position correlation Δx between prompt and delayed event. This information for each event sequence n is represented by the vector $\vec{x}_n = (E_{\mathrm{pr}}, T_{\mathrm{pr}}, E_{\mathrm{del}}, \Delta T, \Delta x)$.

f_{sig} and f_{bg} are the probability density functions for the vector $\vec{x}_n$ in the case of event n being a signal or a background event.

The parameter r describes the signal fraction in the data and is connected to $\sin^2(2\Theta)$ by the linear transformation

$$\sin^2(2\Theta) = \frac{r \cdot N_{\mathrm{sample}}}{N_{\mathrm{sig}}^{\mathrm{exp}}[\sin^2(2\Theta)=1, \Delta m^2]} \tag{15}$$

with the calculated oscillation signal $N_{\mathrm{sig}}^{\mathrm{exp}}[\sin^2(2\Theta) = 1, \Delta m^2]$ for maximal mixing as shown in Fig. 12(a).

Assuming no correlation for the $j=5$ observables of $\vec{x}$, the probability density function is factorized to

$$f_{\mathrm{sig}} = \prod_{j=1}^{5} f_{j,\mathrm{sig}} = f(E_{\mathrm{pr}}, \Delta m^2) \cdot f(T_{\mathrm{pr}}) \cdot f(E_{\mathrm{del}}) \cdot f(\Delta T) \cdot f(\Delta x). \tag{16}$$

Due to the small event sample size of 15 events, the fit is not performed by varying simultaneously the signal and all background components individually. In contrast, the four individual background components are added up to one total background component

$$f_{\mathrm{bg}} = \sum_{i=1}^{4} c_i \cdot \left(\prod_{j=1}^{5} f_{j,\mathrm{bg}_i} \right) \tag{17}$$

with the coefficients c_i being the expected relative contributions of the background channels. The values of c_i are given by the ratio of the expected number of background events N_i of each component and the total background expectation $N_{\mathrm{BG}}^{\mathrm{exp}}$ (see Table III): $c_i = N_i / N_{\mathrm{BG}}^{\mathrm{exp}}$, thereby satisfying the normalization condition $\Sigma_i c_i = 1$.

With the normalization constraint of the probability density function, the parameter r determines also the background contribution in the likelihood maximization

$$N_{\mathrm{bg}} = (1-r) \cdot N_{\mathrm{sample}} \tag{18}$$

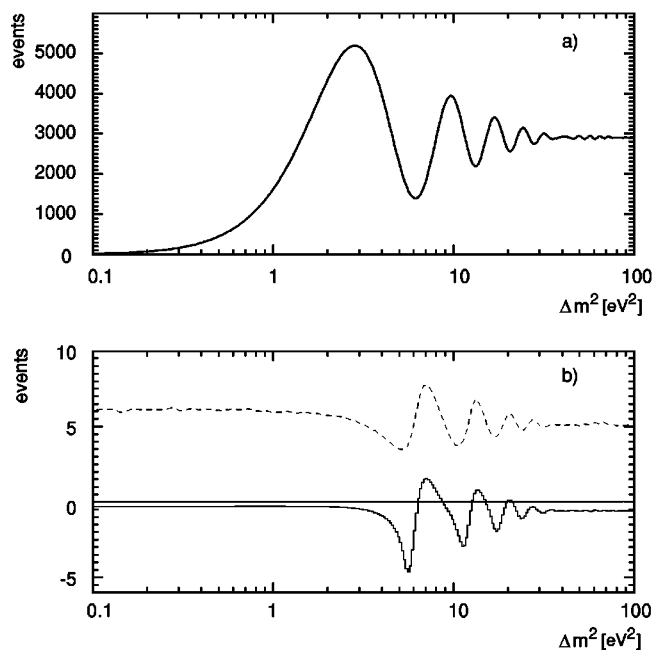

FIG. 12. (a) Expected oscillation signal for maximal mixing $\sin^2(2\Theta) = 1$. (b) Results of the likelihood analysis: The solid line shows the best fit of a $\overline{\nu}_\mu \to \overline{\nu}_e$ signal in the KARMEN 2 data. The dashed line corresponds to the upper bound of the derived 90% confidence interval (C.I.) for an oscillation signal. Note that there is no lower bound of the 90% C.I. for all Δm^2.

TABLE V. Signal event numbers for selected oscillation scenarios. The values of $-\Delta \ln \mathcal{L}$ indicate the difference of the likelihood value to the maximum in the physically allowed region (see text).

Δm^2[eV^2]	$\sin^2(2\Theta)$	$N_{\rm sig}$	$-\Delta \ln \mathcal{L}$
no oscillation		0	0.21
0.1	-1.7×10^{-2}	-0.3	0.21
5.4	-2.4×10^{-3}	-4.4	-0.75
7.0	8.0×10^{-4}	1.5	0.00
100	2.1×10^{-4}	-0.6	0.18

with the above definitions, maximizing $\tilde{\mathcal{L}}$ with regard to $\sin^2(2\Theta)$ and Δm^2 is a pure shape analysis and does not take into account the knowledge of the total background expectation $N_{\rm BG}^{\rm exp}$. To include this quantitative information, the likelihood function is weighted with a Poisson probability term P_P computing the probability of measuring $N_{\rm bg}(r)$ background events for an expectation of $N_{\rm bg}^{\rm exp}$ events:

$$\mathcal{L}(r,\Delta m^2)=\tilde{\mathcal{L}}(r,\Delta m^2)\cdot P_P(N_{\rm bg}(r)|N_{\rm bg}^{\rm exp}) \tag{19}$$

with

$$P_P(N_{\rm bg}(r)|N_{\rm bg}^{\rm exp})=\frac{(N_{\rm bg}^{\rm exp})^{(1-r)N_{\rm sample}}e^{-N_{\rm bg}^{\rm exp}}}{\Gamma[1+(1-r)N_{\rm sample}]}. \tag{20}$$

The expansion in the Poisson probability from the discrete factorial $n!$ to the Gamma function $\Gamma(x)=\int_0^\infty e^{-t}t^{x-1}dt$ with $\Gamma(n+1)=n!$ ensures a continuous calculation of the Poisson probability for any signal ratio r.

Maximizing the above defined likelihood function $\mathcal{L}$ for the final KARMEN 2 data results in a best fit for r compatible with the no-oscillation solution. In fact, the global maximum of $\mathcal{L}$ is reached slightly in the unphysical region, at oscillation parameters

$$\sin^2(2\Theta)=-2.4\times10^{-3}, \qquad \Delta m^2=5.4 \ \ {\rm eV}^2. \tag{21}$$

Restricting the analysis to the allowed region, the likelihood function is found to be maximal at

$$\sin^2(2\Theta)=8.0\times10^{-4}, \qquad \Delta m^2=7.0 \ \ {\rm eV}^2. \tag{22}$$

Table V shows the number of (e^+,n) sequences from $\bar{\nu}_\mu \to \bar{\nu}_e$ oscillations of some selected parameter combinations k. Also given are the differences of the likelihood values to the maximum in the physically allowed region $-\Delta \ln \mathcal{L}=\ln \mathcal{L}_k - \ln \mathcal{L}_{\rm max}$. The logarithmic likelihood value of the best fit differs from the likelihood value for no oscillation by only 0.21 units. As will be discussed in Sec. VII B, a statistical analysis of the likelihood function indicates that for boundaries of 90% confidence intervals (C.I.), typical differences of $-\Delta \ln \mathcal{L}\approx 4-5$ have to be applied. This underlines the fact that the maximum at $[\sin^2(2\Theta),\Delta m^2]_{\rm max}=(8.0\times10^{-4},7.0 \ \ {\rm eV}^2)$ is statistically in excellent agreement with the null hypothesis of no oscillations.

Furthermore, simulations of comparable event ensembles, with no oscillation signal but background only, show that a global maximum at slightly unphysical oscillation parameters as it is in case here [Eq. (21)] is a typical result of the likelihood analysis of small event samples $\langle N_{\rm sample}\rangle=15.8$.

Figure 12(a) shows the expected oscillation event numbers as a function of Δm^2 for maximal mixing $\sin^2(2\Theta)=1$. In contrast, Fig. 12(b) demonstrates the results of the maximum likelihood analysis. For 90 slices per decade in Δm^2, the number of oscillation events for maximal likelihood $N_{\rm sig}^{\rm max}$ is plotted (solid histogram). For low as well as high values of Δm^2, the corresponding best fits are almost identical with the physical boundary, with values of $N_{\rm sig}^{\rm max}=-0.3$ and $N_{\rm sig}^{\rm max}=-0.6$, respectively. In a region of about $3\leqslant\Delta m^2 \leqslant 30$ eV^2, stronger variations of the energy spectrum of a potential signal come into play: Since KARMEN has an excellent energy resolution of $\sigma_E\approx2\%$ for positrons with $E \approx 30$ MeV, statistical variations in $E_{\rm pr}$ of the small event sample can be easily interpreted by the likelihood analysis as modification of the background energy spectrum due to oscillations with an oscillation length comparable to the distance target detector

$$L_{\rm osc}=\frac{2\pi\cdot E}{1.27\cdot\Delta m^2}\approx17 \ \ {\rm m}. \tag{23}$$

For energies $12\leqslant E(\bar{\nu}_\mu)\leqslant 52.8$ MeV, Eq. (23) leads to oscillation parameters of about $3\leqslant\Delta m^2\leqslant15$ eV^2 [58]. It is important to note that the results given in Fig. 12(b) for $3 \leqslant\Delta m^2\leqslant30$ eV^2 are statistically perfectly compatible with the no-oscillation solution, as will be discussed in the next section.

B. Upper limits on oscillation parameters

Finally, the confidence intervals for the parameters $\sin^2(2\Theta)$ and Δm^2 have to be deduced from the experimental likelihood function. Recently, there have been discussions [59] about various approaches in order to obtain confidence regions, especially under the aspects of event samples of low statistics, oscillatory behavior of the likelihood function, as well as parameter determination near physical boundaries. In the following, we adopt the unified approach [60] which is a frequentist approach with a specific ordering principle: In the $[\sin^2(2\Theta),\Delta m^2]$ plane, a 2-dimensional confidence interval (C.I.) for the oscillation parameters is constructed from the comparison of the experimental likelihood value $\Delta \ln \mathcal{L} =\ln \mathcal{L}[\sin^2(2\Theta),\Delta m^2]-\ln \mathcal{L}[\sin^2(2\Theta),\Delta m^2]_{\rm max}$ with the outcome of a large sample of Monte Carlo simulations of so-called toy experiments for this term. These simulations are based on the detailed knowledge of all resolution functions and the spectral information on the background. In addition, they comprise the expected experimental signal for an oscillation hypothesis with given parameters $[\sin^2(2\Theta),\Delta m^2]$. The hypothesis is then accepted in the 90% C.I. if the experimental value does not lie within the outer 10% tail of the simulated $-\Delta \ln \mathcal{L}$ distribution. For a complete statistical analy-

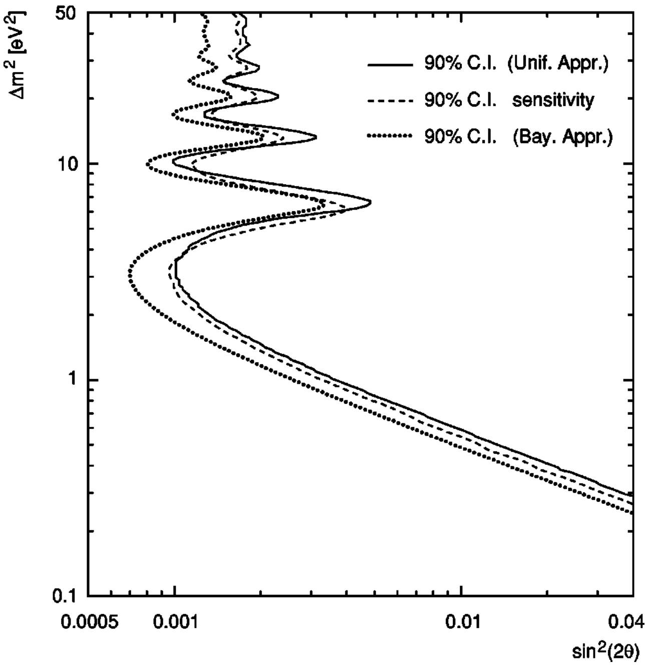

FIG. 13. KARMEN 2 90% C.I. result deduced with the unified approach (solid), 90% C.I. sensitivity within the unified approach (dashed), and 90% C.I. in the Bayesian approach (dotted). Regions to the right of the curves are excluded. Note the zoom of the axis in $\sin^2(2\Theta)$, not reaching up to 1.

sis, the entire parameter space $[\sin^2(2\Theta),\Delta m^2]$ is scanned to extract the according region of confidence.

In Fig. 12(b), the result of this approach is shown in terms of excluded oscillation events. The dashed line corresponds to the limit of the 90% confidence interval, excluding larger signal event numbers. For $\Delta m^2 = 100$ eV^2 an oscillation signal stronger than 5.1 events is excluded in the 90% C.I., while for low $\Delta m^2 < 0.1$ an oscillation signal larger than 6.0 events is excluded. Though one of the major features of the unified approach is the possibility of extracting lower limits within the same analysis, no *lower* limit of the 90% C.I. appears, demonstrating the compatibility of the likelihood result with the no-oscillation hypothesis regardless of the chosen value for Δm^2.

The exclusion plot in the 2-dimensional $[\sin^2(2\Theta),\Delta m^2]$ plane (Fig. 13) is derived by dividing, for all values of Δm^2, the excluded events [see the solid line in Fig. 12(b)] by the expectation for maximal mixing [Fig. 12(a)]. This results in the 90% C.I. limits

$$\sin^2(2\Theta) < 1.7\times 10^{-3}, \qquad \Delta m^2 \geqslant 100 \ \text{eV}^2, \qquad (24)$$

$$\Delta m^2 < 0.055 \ \text{eV}^2, \qquad \sin^2(2\Theta) = 1. \qquad (25)$$

The entire exclusion curve is shown in Fig. 13 as solid line, excluding parameter combinations in the area right to the curve.

An important criterion of an experimental result and a derived upper limit is the question of how close the limit quoted is to the experimental sensitivity. Following Ref. [60], the sensitivity is defined as expectation value for the upper limit of the 90% confidence interval under the assumption of no oscillations and is gained by simulations of experiments' outcomes. The KARMEN 2 sensitivity as a function of Δm^2 is shown in Fig. 13 as a dashed line. The sensitivity $\langle \sin^2(2\Theta)\rangle$ for $\Delta m^2 = 100$ eV^2 amounts to

$$\langle \sin^2(2\Theta)\rangle = 1.6\times 10^{-3} \quad 90\%\text{C.I.} \qquad (26)$$

For completeness, we also perform a Bayesian approach to derive an upper limit on the oscillation parameters $\sin^2(2\Theta)$ and Δm^2 . In the Bayesian framework, the upper limits for fixed Δm^2 are obtained by integrating the likelihood function $\mathcal{L}$. This integration implies the use of a prior probability density distribution for $\sin^2(2\Theta)$ [61] and decomposes the 2-dimensional problem into a one-dimensional treatment. We used a uniform prior in a logarithmic metric of the oscillation parameter $\sin^2(2\Theta)$. In both the frequentist and Bayesian approaches, we restrict the parameter space to the physically allowed region. The Bayesian 90% C.I. approach yields more stringent upper limits shown as dotted line in Fig. 13 with

$$\sin^2(2\Theta) < 1.3\times 10^{-3} \quad \Delta m^2 \geqslant 100 \ \text{eV}^2. \qquad (27)$$

Because of the ambiguities in choosing the probability density distribution for $\sin^2(2\Theta)$ as well as the 2-dimensional oscillatory behavior of the likelihood function, we do not favor the Bayesian extraction of confidence intervals but refer to the results deduced within the frequentist unified approach [see Eq. (24)]. The resemblance of the KARMEN exclusion curve with its sensitivity curve underlines the fact, that the likelihood analysis results in no indication of a $\bar{\nu}_\mu \to \bar{\nu}_e$ oscillation signal in the KARMEN 2 data.

C. Comparison with LSND and other experiments

The parameter space for oscillations $\bar{\nu}_\mu \to \bar{\nu}_e$ excluded at 90 % C.I. by the KARMEN 2 measurement is shown in Fig. 14. The KARMEN result sets the most sensitive limits so far on $\bar{\nu}_\mu \to \bar{\nu}_e$ oscillations in the parameter region of $0.3 \leqslant \Delta m^2 \leqslant 30$ eV^2 . At higher Δm^2 values, the area right to the exclusion curve is also excluded by a combined $\nu_\mu \to \nu_e$ and $\bar{\nu}_\mu \to \bar{\nu}_e$ search of CCFR [62]. The search for $\bar{\nu}_e$ disappearance at the Bugey reactor [63] excludes small Δm^2 values, at large amplitudes $A > 0.03$ [64]. The parameter area excluded by KARMEN covers large parts of the parameter combinations favored by the LSND experiment [7]. The LSND result plotted here shows areas obtained by cutting the experiment's logarithmic likelihood function at constant values 2.3 and 4.6 units below the likelihood maximum [12]. For values of $\Delta m^2 \leqslant 2$ eV^2 , the oscillation signal expected in KARMEN based on the LSND region ($\ln \mathcal{L}_{\max} - 2.3$) corresponds to a range of 3 to 14 oscillation events. As shown in Fig. 12, a signal larger than 6 events is excluded at 90% C.L. At $\Delta m^2 \geqslant 20$ eV^2 , the expected LSND signal of 7 to 13 oscillation events in KARMEN is in clear contradiction to the KARMEN upper limit of 5.1 (6.5) events at 90% C.I. (95% C.I.).

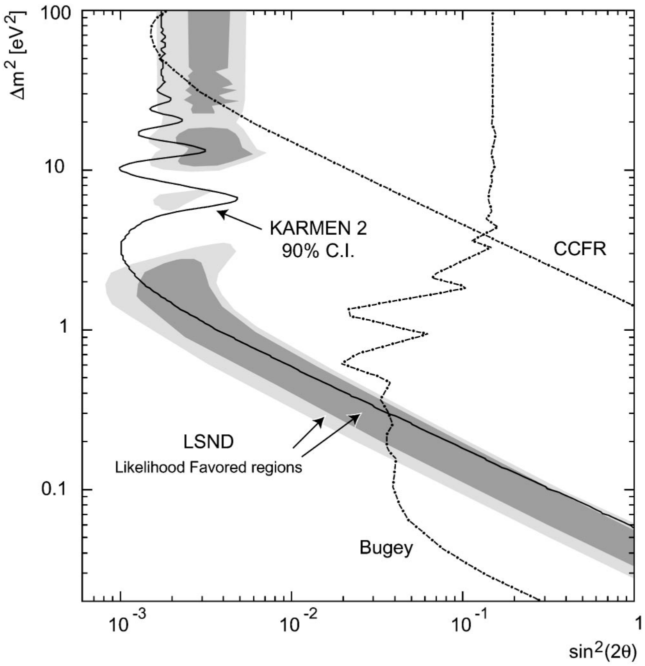

FIG. 14. Comparison of oscillation searches performed by different short baseline experiments.

These examples based on expected additional $\bar{\nu}_e$ events from $\bar{\nu}_\mu \rightarrow \bar{\nu}_e$ demonstrate that at smaller values of Δm^2 there is a restricted parameter region statistically compatible with both experimental results. At high Δm^2 values, the LSND solutions are in clear contradiction with the KARMEN upper limit.

VIII. CONCLUSION

Results based on the entire KARMEN2 data set collected from 1997 through 2001 have been presented. The extracted candidate events for $\bar{\nu}_e$ are in excellent agreement with background expectations showing no signal for $\bar{\nu}_\mu \rightarrow \bar{\nu}_e$ oscillations. A detailed likelihood analysis of the data leads to upper limits on the oscillation parameters $\sin^2(2\Theta)$ and Δm^2 excluding parameter regions not explored analyzed by other experiments.

These limits exclude large regions of the parameter area favored by the LSND experiment. A more quantitative statistical statement on the compatibility between KARMEN and LSND has to be based on a combined statistical analysis of both likelihood functions [65]. Such a detailed joint statistical analysis has been performed [66].

The negative search for $\bar{\nu}_e$ from muon decay at rest presented here sets also stringent limits on other potential processes of $\bar{\nu}_e$ production such as lepton family number violating decays $\mu^+ \rightarrow e^+ + \bar{\nu}_e + \nu_\mu$ or neutrino oscillations $\nu_e \rightarrow \bar{\nu}_e$ which will be discussed in a separate paper. Future experiments such as the MiniBooNE experiment at Fermilab [67] aim at investigating the LSND evidence and the oscillation parameters not yet excluded by the $\bar{\nu}_\mu \rightarrow \bar{\nu}_e$ search presented here.

ACKNOWLEDGMENTS

We gratefully acknowledge the financial support from the German Bundesministerium für Bildung und Forschung (BMBF), the Particle Physics and Astronomy Research Council (PPARC), and the Council for the Central Laboratory of the Research Councils (CCLRC). In particular, we thank the Rutherford Appleton Laboratory and the ISIS neutron facility for hospitality and steady support during years of data taking.

[1] For a review see, e.g., M.F. Altmann *et al.*, Rep. Prog. Phys. **64**, 97 (2001).
[2] Q.R. Ahmad *et al.*, Nucl. Instrum. Methods Phys. Res. A **449**, 172 (2000).
[3] Q.R. Ahmad *et al.*, Phys. Rev. Lett. **87**, 071301 (2001).
[4] J.N. Bahcall, Phys. Rev. C **65**, 015802 (2002).
[5] For a review see, e.g., T. Kajita and Y. Totsuka, Rev. Mod. Phys. **73**, 85 (2001); J.G. Learned, in *Current Aspects of Neutrino Physics*, edited by D. Caldwell (Springer Verlag, Berlin, 2001).
[6] S. Fukuda *et al.*, Phys. Rev. Lett. **85**, 3999 (2000).
[7] C. Athanassopoulos *et al.*, Nucl. Instrum. Methods Phys. Res. A **388**, 149 (1997).
[8] C. Athanassopoulos *et al.*, Phys. Rev. Lett. **75**, 2650 (1995).
[9] C. Athanassopoulos *et al.*, Phys. Rev. Lett. **81**, 1774 (1998).
[10] C. Athanassopoulos *et al.*, Phys. Rev. C **54**, 2685 (1996).
[11] C. Athanassopoulos *et al.*, Phys. Rev. Lett. **77**, 3082 (1996).
[12] A. Aguilar *et al.*, Phys. Rev. D **64**, 112007 (2001).
[13] D. Suematsu, Phys. Lett. B **392**, 413 (1997).
[14] Z.G. Berezhiani and R.N. Mohapatra, Phys. Rev. D **52**, 6607 (1995).
[15] R. Foot and R.R. Volkas, Phys. Rev. D **52**, 6595 (1995).
[16] O. Haug, A. Faessler, and J.D. Vergados, J. Phys. G **27**, 1743 (2001).
[17] G. Barenboim *et al.*, Phys. Rev. D **65**, 053001 (2002).
[18] B.E. Bodmann *et al.*, Phys. Lett. B **332**, 251 (1994).
[19] B.E. Bodmann *et al.*, Phys. Lett. B **339**, 215 (1994).
[20] B. Armbruster *et al.*, Phys. Lett. B **423**, 15 (1998).
[21] B. Zeitnitz *et al.*, Prog. Part. Nucl. Phys. **40**, 169 (1998).
[22] B. Armbruster *et al.*, Phys. Rev. C **57**, 3414 (1998).
[23] B. Armbruster *et al.*, Phys. Lett. B **348**, 19 (1995).
[24] K. Eitel, Forschungszentrum Karlsruhe Scientific Report No. FZKA 5684, 1995.
[25] B. Armbruster *et al.*, Phys. Rev. Lett. **81**, 520 (1998).
[26] R.L. Burman *et al.*, Nucl. Instrum. Methods Phys. Res. A **368**, 416 (1996).
[27] G. Drexlin *et al.*, Nucl. Instrum. Methods Phys. Res. A **289**, 490 (1990).

[28] J. Wolf, Forschungszentrum Karlsruhe Scientific Report No. FZKA 5636, 1995.
[29] Z. Maki, M. Nakagawa and S. Sakata, Prog. Theor. Phys. **28**, 870 (1962).
[30] B.W. Lee *et al.*, Phys. Rev. Lett. **38**, 937 (1977).
[31] G. Fogli *et al.*, Phys. Rev. D **52**, 5334 (1995); **56**, 3081 (1997).
[32] S.M. Bilenky *et al.*, Phys. Lett. B **356**, 273 (1995); **54**, 1881 (1996).
[33] K.S. Babu *et al.*, Phys. Lett. B **359**, 351 (1995).
[34] E. Torrente-Lujan, Phys. Lett. B **389**, 557 (1996).
[35] H. Minakata, Phys. Rev. D **52**, 6630 (1995).
[36] S. Barshay and P. Heiliger, Astropart. Phys. **6**, 323 (1997).
[37] C.Y. Cardall and G.M. Fuller, Phys. Rev. D **53**, 4421 (1996).
[38] B. Kayser and R.N. Mohapatra, in *Current Aspects of Neutrino Physics*, edited by D. Caldwell (Springer Verlag, Berlin, 2001), and references therein.
[39] P. Vogel and J.F. Beacom, Phys. Rev. D **60**, 053003 (1999).
[40] D.H. White and T.A. Siddiqi, Nucl. Phys. **A217**, 410 (1973).
[41] The n capture on ^{157}Gd with a cross section of $\sigma=254000\times10^{-24}$ cm^2 and an end point energy of $E_0=7937.4$ keV [40] dominates over the n capture on other Gd isotopes.
[42] M.E. Plett and S.E. Sobottka, Phys. Rev. C **3**, 1003 (1971).
[43] R. Brun *et al.*, GEANT—*Detector Description and Simulation Tool* (CERN, Geneva, 1993).
[44] C. Zeitnitz, Nucl. Instrum. Methods Phys. Res. A **349**, 106 (1994).
[45] T. Suzuki *et al.*, Phys. Rev. C **35**, 2212 (1987).
[46] T. Jannakos, Forschungszentrum Karlsruhe Scientific Report No. FZKA 5520, 1995.
[47] E. Kolbe and K. Langanke, Phys. Rev. C **63**, 025802 (2001).
[48] T. Suzuki, D.F. Measday, and J.P. Roalsvig, Phys. Rev. C **35**, 2212 (1987).
[49] B. Armbruster, Forschungszentrum Karlsruhe Scientific Report No. FZKA 6102, 1998.
[50] R.L. Burman, KARMEN technical note, 1994.
[51] E. Kolbe, in Proceedings of the Fifth International Symposium on Nuclear Astrophysics, NIC V, Volos, Greece, 1998.
[52] This number is valid for the final data cuts given in Sec. VI.
[53] R.L. Burman and P. Plischke, Forschungszentrum Karlsruhe Scientific Report N. FZKA 5595, 1995.
[54] G.J. Russel, in Proceedings of International Collaboration on Advanced Neutron Sources, Tsukuba, 1990.
[55] The μSR (muon spin resonance) target is located in the ISIS beam line upstream of the main target at a distance of 29.2 m to the KARMEN detector.
[56] Particle Data Group, R.M. Barne *et al.*, Phys. Rev. D **54**, 1 (1996).
[57] O. Helene, Nucl. Instrum. Methods **212**, 319 (1983).
[58] In more detail, this argument is extended to the second oscillation mode, with $L_{\mathrm{osc},2}\approx17/2=8.5$ m, which explains the variation up to values of about $\Delta m^2\leqslant30$ eV^2, as can be seen in Fig. 12.
[59] F. James, L. Lyons, and Y. Perrin, Proceedings of Workshops on Confidence Limits, CERN-Report No. 2000-005, 2000.
[60] G.J. Feldman and R.D. Cousins, Phys. Rev. D **57**, 3873 (1998).
[61] D.E. Groom *et al.*, Eur. Phys. J. C **15**, 1 (2001).
[62] A. Romosan *et al.*, Phys. Rev. Lett. **78**, 2912 (1997).
[63] B. Achkar *et al.*, Nucl. Phys. **B434**, 503 (1995).
[64] Note that, in a complete 3- or 4-neutrino mixing scenario, due to the $\bar{\nu}_e$ disappearance search of Ref. [63] the oscillation amplitude describes a combination of mixing angles different from that of $\bar{\nu}_\mu\rightarrow\bar{\nu}_e$ appearance experiments such as KARMEN and LSND (see, e.g. Ref. [31]).
[65] K. Eitel, New J. Phys. **2**, 1.1 (2000).
[66] E. Church *et al.*, Phys. Rev. D (to be published).
[67] A.O. Bazarko *et al.*, Nucl. Phys. B (Proc. Suppl.) **91**, 210 (2001).